Nanoscale

PAPER

View Article Online
View Journal | View Issue

Cite this: *Nanoscale*, 2022, **14**, 13561

A nanoarchitecture of a gold cluster conjugated gold nanorod hybrid system and its application in fluorescence imaging and plasmonic photothermal therapy†

Resmi V. Nair,[a,b] Muhammed Fasil Puthiyaparambath,[c] Raghu Chatanathodi,[c] Lakshmi V. Nair*[b] and Ramapurath S. Jayasree*[a]

Received 8th June 2022,
Accepted 18th August 2022

DOI: 10.1039/d2nr03163a

rsc.li/nanoscale

Engineering different nanomaterials into a single functional material can impart unique properties of the parental nanoparticles, especially in the field of bio imaging and therapy. Gold nanomaterials having different sizes, shapes and dimensionalities exhibit exceptional properties apart from their non-toxicity and hence are strong candidates in the biomedical field. Designing a hybrid nanomaterial of two gold nanostructures retaining the individual properties of the parental nanomaterials is challenging. Here, we demonstrate the synthesis of a hybrid nanomaterial (GQC@GNR), comprising an extremely small gold nanocluster and a representative of the asymmetric gold nanostructure, *i.e.*, a gold nanorod, both having their own different exclusive optical properties like tuneable emission and NIR absorption characteristics, respectively. The hybrid system is designed to retain its emission and absorption in the NIR region to use it as an agent for simultaneous imaging and therapy. The formation of GQC@GNR and its architectonics heavily depend on the synthesis route and the parameters adopted which in turn have a direct influence on its properties. The architecture and its connection to the optical properties are explained using UV-Vis absorption and photoluminescence spectroscopy, zeta potential, transmission electron microscopy, *etc.* DFT-based computational modelling supports architectonics as explained by the experimental findings. The formation of the gold–gold hybrid system witnessed interesting science with a strong indication that materials with desired properties can be designed by appropriately modulating the architectonics of hybrid formation. Finally, folate conjugated GQC@GNR demonstrated its efficacy for targeted imaging and photothermal therapy in HeLa cells and tumor-bearing animal models. The detailed therapeutic efficacy of GQC@GNR is also explained based on Raman spectroscopy.

Introduction

Fabrication of functional materials *via* chemical reactions, and manipulation at the atomic and molecular level are one of the promising methods to create and evaluate various living and non-living systems.[1,2] Nanotechnology allows creation of different architectonics of materials by suitably arranging atoms and molecules and has been explored in different science and technological ventures. For example, the arrangement of carbon atom in different bondings can gain separate forms like carbon nanotubes (CNTs), graphene, diamond, *etc.*[3,4] The DNA sequence formed by the combination of adenine, thymine, guanine and cytosine subunits is also an example of architectonics formed by the arrangement of basic subunits. Apart from this classic architectonic assembly, a plasmonic nanoparticle assembly was extensively studied by Choi *et al.* using dopamine.[5,6] On the other hand, metal clusters are formed by the suitable arrangement of metal atoms stabilized with ligands. The size of these metal clusters lies between that of a nanoparticle and an atom. Clusters generally form different structural motifs such as icosahedral, cuboctahedral, *etc.*[7] They are a group of sub-nanometer particles following unique architectonics of gold atoms and possess fluorescence emission properties[8,9] due to quantum confinement.[10–13] Gold quantum clusters are comprised of a few atoms of gold and show molecular like behavior.[10–14]

---

[a] *Division of Biophotonics and Imaging, Sree Chitra Tirunal Institute of Medical Sciences and Technology, Trivandrum, 695012, India. E-mail: jayasree@sctimst.ac.in*
[b] *School of Materials Science and Engineering, National Institute of Technology Calicut, 673601 Kerala, India. E-mail: lakshmivnair@nitc.ac.in*
[c] *Department of Physics, National Institute of Technology Calicut, Kerala, India*

† Electronic supplementary information (ESI) available: Emission and absorption spectra, FT-IR spectra, quantum yields, temperature generation and zeta potential measurements, UV-visible spectra, cytotoxicity, *in vitro* PTT and *ex vivo* images of the organs of mice. See DOI: **https://doi.org/10.1039/d2nr03163a**

Metallic nanomaterials show size, shape and architectonics-dependent photophysical properties, which make them suitable for application in the fields of optoelectronics, biomedicine, catalysis, *etc.*[15] Different sized and shaped metallic nanomaterials have been synthesized and evaluated for their efficacy in various applications.[16–20] Another metallic nanomaterial that we considered is gold nanorods which have attracted wide attention because of their unique shape, structure and surface plasmon absorption in the NIR range with high efficacy to convert light into heat (photo thermal properties). Surface modifications of metallic nanomaterials are one of the important factors that determine their properties.[21–23] Surface modification of cetyltrimethylammonium bromide (CTAB)–gold nanorods (GNRs) is one of the mostly studied areas.[24–26] To impart additional properties and/or to decrease the toxicity, different coatings such as polymers, bifunctional molecules, dye molecules and biomolecules have been explored.[27–32] Apart from these, coating with other metal nano particles (SiO_2, Pt, and Fe) has also been established.[33–37]

Surface modification of GNRs with gold quantum clusters will impart better performance in terms of their biocompatibility and varied properties. Moreover, combining a gold nanorod with gold clusters will help to study the interaction of different functional materials of the same atoms like gold. Such systems will help to improve the overall performance by overcoming the limitations offered by conventional individual systems. The so developed materials can also reduce the toxicity of GNRs to a great extent. They can be used as a target in the fields of bioimaging and therapy. To the best of our knowledge, there are no such attempts on the development of a functional nanomaterial using GNRs and gold quantum clusters. Here, we report an optimized method for the development of hybrid GNR–gold quantum clusters for bio imaging and therapeutic application *in vivo*. We have also explained the nanoarchitectonics of the hybrid system in the context of desired optical and thermal properties.

Experimental section

Materials

Chloroauric acid ($HAuCl_4$), cetyltrimethylammonium bromide (CTAB), reduced glutathione, mercaptosuccinic acid, and folic acid were purchased from Sigma Aldrich. Sodium borohydride, silver nitrate, ascorbic acid, and sodium hydroxide were purchased from Merck. All cell culture media (DMEM) and reagents (MTT, acridine orange, ethidium bromide, DAPI (4′,6-diamidino-2-phenylindole), FBS, and antibiotic–antimycotic solution) were purchased from HiMedia.

The water used in the entire study was ultrapure water (18.2 MΩ cm). All glassware was washed with aqua regia, rinsed with distilled water followed by ultrapure water, and dried in an oven. All the chemicals are commercially available and used without any further purification unless stated.

Synthesis of the gold nanorod. The seed-mediated synthesis method was used for the preparation of GNR. Initially, 2.2 mM (250 μL) chloroauric acid ($HAuCl_4$) solution was treated with 3 mL of 0.1 M cetyltrimethylammonium bromide (CTAB) followed by reducing with 10 mM (100 μL) sodium borohydride ($NaBH_4$) to form a seed solution. The resultant solution was maintained for 3 h at 20 °C for uniform seed growth. GNR growth solution was prepared by mixing 2.2 mM (2.5 mL) of $HAuCl_4$ with 0.1 M (50 mL) CTAB followed by the addition of 0.01 M (250 μL) $AgNO_3$ and 0.1 M (250 μL) ascorbic acid. Then 200 μL of seed was added to this solution and mixed well; the solution was kept for 24 h in the dark. Excess of CTAB was removed from the GNR solution by refrigerating the resultant solution followed by keeping it at room temperature. The CTAB particles settle down and are removed by collecting the supernatant. The supernatant was centrifuged at 12 000 rpm for 20 minutes thrice to obtain GNR.[31,32] GNR was treated with 1 mL of 10 M HCl at 60 °C for 4 h with 520 rpm stirring speed to obtain surface active HGNR. HGNR was collected by centrifugation at 14 000 rpm.

Gold nanocluster. Gold nanoclusters (GQC) were synthesised using two-step top-down approach. In the first step gold nanoparticles, GMSA, were synthesised; briefly, 49 mg of $HAuCl_4$ and 39 mg of MSA were dissolved in 25 mL of Milli-Q water and allowed to react for 30 minutes. Then 0.2 M sodium borohydride was added at 0 °C and allowed to react for 1 h. The product obtained was brown in color and it was precipitated in methanol and collected by a four-step centrifugation process to obtain the gold nanoparticle (GMSA). The GMSA formed was the base material for the synthesis of the gold cluster. GMSA was etched using reduced glutathione (GSH) for the same. For this, 2.8 mg of GMSA was treated with 12 mg of GSH in 30 mL of water at a pH of 1.5 at 0 °C temperature. After 15 min, the temperature of the system was increased to 70 °C and stirred at a speed of 500 rpm which continued for 24 h. The color change from brown to light yellow indicates the formation of a gold cluster. GQC was collected by centrifugation at 3000 rpm to remove bigger particles, followed by precipitation of the supernatant in 1 : 1 methanol isopropanol.[38,39]

Synthesis of the gold nanocluster–gold nanorod hybrid nanomaterial. While synthesising the GQC–GNR hybrid, we have chosen three different conditions to control the architectonics of the final system to suit the intended use. For this, three different hybrid systems were developed using the GQC of different pH values to synthesise the hybrid system. GQCs under different pH conditions [7 (neutral-NGQC), 3 (acidic-AGQC), and 12 (basic-BGQC)] were added to HGNR (pH 7) with mass ratio 1 : 2. The pH of the cluster was varied using sodium hydroxide or dilute hydrochloric acid. The three mixtures were stirred for 3 h. Afterwards, purification was performed by centrifugation.

Synthesis of FA–NGQC@GNR. 0.05 mg mL^{-1} folic acid was treated with 5 mg of 1-ethyl-3-[3-dimethylaminopropyl]carbodiimide hydrochloride (EDC) in 0.5 mL water followed by 3 mg 0.5 mL^{-1} *N*-hydroxysuccinimide for 3 h. To this 1 mg mL^{-1}

NGQC@GNR was added dropwise and the reaction was continued for another 2 h. The material was purified by centrifugation at 14 000 rpm

Characterization

Absorbance spectra (Shimadzu UV spectrometer-UV 2600) and emission spectra (Varian Carl Eclipse fluorescence spectrophotometer) were recorded to study the optical properties of the synthesised materials. Zeta potential measurement was performed to check surface functionalization using a Malvern Zetasizer Nano ZS 90. TEM analysis was performed using a 100 kV (JEM-2010 HiTachi-JEOL, Tokyo, Japan) electron microscope. *In vivo* animal imaging efficacy of the developed material was monitored using a Xenogen IVIS Spectrum.

Computational study. DFT calculations were performed using the Vienna *Ab initio* Simulation Package (VASP).[40,41] The Perdew–Burke–Ernzerhof (PBE)[42] functional within the generalized gradient approximation (GGA) was used for the exchange–correlation functional. The bulk lattice parameter of Au obtained from computations is 4.16 Å, which agrees well with the experimental results.[43] For modelling GNR, we used an Au(111) surface with a 7 × 6 supercell with 4 layers. To avoid the interaction between periodic images, a vacuum space of 20 Å was set along the *c*-axis. The plane wave cut-off energy was set to 400 eV. For sampling the Brillouin zone, a 15 × 15 × 15 Monkhorst–Pack grid[44] was used for the bulk, and a 3 × 3 × 1 for slab calculations. Total electronic energies were converged to within 10^{-5} eV.

The interaction of the GQC with GSH was modelled using a three atom Au cluster. The molecule like GQC–GSH hybrid was optimized in a cubic box of 20 Å. GQC–GSH was then placed atop an Au atom of GNR. We have considered two modes of binding of GQC–GSH with the Au surface, one in which an O atom of GQC–GSH binds atop an Au (named Conf-1) and the other in which the N atom of GQC–GSH binds atop Au (named Conf-2). The adsorption energy of the GQC–GSH cluster to the GNR surface was calculated using the equation $E_{\text{ads}} = E_{\text{Sys}} - E_{\text{slab}} - E_{\text{GQC–GSH}}$, where E_{Sys}, E_{slab} and $E_{\text{GQC–GSH}}$ are the total energy of the combined system (GQC@GNR), energy of GNR and energy of isolated GQC–GSH, respectively.

Evaluation of temperature generation. 1 mg mL^{-1} of GNR, AGQC@GNR, BGQC@GNR and NGQC@GNR were dissolved in water in a glass vial. An 808 nm diode laser with 0.05 W power was used to irradiate the vial from the bottom. The time dependent increase in the temperature was monitored using a thermocouple module of Metravi DT-19RS.

***In vitro* cytotoxicity.** A mouse fibroblast cell line, L929, and human cancer cells, HeLa cells, were used for *in vitro* cytotoxicity studies to check the action of the material in normal and cancer cells, respectively. The cells (9000 cells per well) were seeded in 96 well plates and incubated for 24 h. Wells with media alone were used as controls. The media were replaced with media containing test materials (100 μL). After 48 h of incubation, the media were removed and 100 μL of fresh DMEM containing 3-(4,5-dimethylthiazol-2-yl)-2,5-diphenyltetrazolium bromide (MTT-10 μl, 5 mg mL^{-1}) was added to it. Insoluble MTT formazan crystals were formed after 4 h of incubation. Using a microplate reader (Synergy H1 hybrid multi-mode microplate reader, Bio-Tek) the absorbance at 570 nm was measured. By comparing with control cells, the percentage cell viability of cells in the presence of a hybrid material was calculated.

Cell uptake of FA–NGQC@GNR. Fluorescence microscopy (IX83; Olympus, Tokyo, Japan) images of HeLa cells were taken after incubation with the FA–NGQC@GNR nano hybrid for 3 h. Images were captured with green (FITC) excitation and far-red emission (HcRed) filters corresponding to nanohybrid emission properties.

Evaluation of photothermal therapy in cells. Human cancer cells (HeLa cells) were used for photothermal evaluation. Different concentrations (0.5 mg mL^{-1}, 0.4 mg mL^{-1}, 0.3 mg mL^{-1}, 0.2 mg mL^{-1}, 0.1 mg mL^{-1}, 0.05 mg mL^{-1} and 0.025 mg mL^{-1}) of folic acid conjugated NGQC@GNR in cell culture medium and 100 μL of the same were added on pre-seeded cells by replacing the media. Cells without the material were considered as controls. Then an 808 nm laser with 0.05 W power was used to irradiate for 60 s followed by MTT assay to assess the temperature dependent cell death.

Qualitative evaluation of photothermal therapy was carried out using live/dead assay performed using ethidium bromide and acridine orange for staining the live and dead cells, respectively. The cells were treated with 0.5 mg mL^{-1} of the developed hybrid nanomaterial for 3 h, washed with PBS and then irradiated with an 808 nm laser. After laser irradiation, the cells were again washed with PBS and stained with ethidium bromide and acridine orange. Microscopic images of treated wells were taken with blue and green excitation filters.

***In vivo* imaging.** All animal procedures were performed in accordance with the guidelines set by the Committee for the Purpose of Control and Supervision of Experiments on Animals (CPCSEA), Government of India and were approved by the Institutional Animal Ethics Committee of Sree Chitra Tirunal Institute for Medical Sciences and Technology.

Dalton's lymphoma cells were injected subcutaneously into the hind flank of each of Swiss albino mouse weighing 30 g each. When the tumor volume is sufficiently large to visualize, animals were used for experiments (after 5 days).

Tumor bearing mice were divided into two groups. Animals of the control group were injected with PBS. The second group of animals were injected with 0.5 mg mL^{-1} of FA–NGQC@GNR in 500 μL of PBS intravenously. After 30 min, the animals were imaged using an IVIS Spectrum animal imaging system. Representative animals from each group were euthanized, and images were collected from excised organs to monitor the biodistribution of the materials in various organs.

Results and discussion

In order to develop a hybrid nanomaterial, parental materials such as gold nanorods (GNRs) and glutathione stabilized gold clusters (GQCs) were synthesized as per the optimized protocol reported by our group.[31,32,38,39] The broad fluorescence emission in the NIR range around 750 nm (Fig. S1a†) is attributed to the glutathione cluster, Au33 as reported earlier.[45] The GNR shows characteristic longitudinal and transverse absorption peaks around 710 and 530 nm (Fig. 1a and Fig. S1b†) respectively.

The transmission electron micrograph of the gold nanorod showed an aspect ratio of 3.3, whereas GQC has a size of around 0.7 nm with a well dispersed pattern (Fig. S2†). The as synthesized GNR is treated with HCl to produce surface active GNR (HGNR) by removing the surface bound cetyltrimethylammonium bromide (CTAB). This step is also expected to avoid the fluorescence quenching when the hybrid system is formed. HCl treatment was continued until the absorbance became broader. A gold to gold based functional hybrid system was designed to evaluate the photophysical properties based on its architecture and subsequent use for bioimaging and targeted therapy *in vivo.*

To understand the hybrid nanomaterial formation with the best properties, gold clusters under different pH conditions (neutral, acidic and basic) were mixed with neutral HGNR and the resultant products are represented as NGQC@GNR, AGQC@GNR and BGQC@GNR, respectively. The optimized reaction procedure for the synthesis of the sample is shown in Scheme 1. Briefly, the pH of GQC was changed to acidic, neutral and basic using 0.001 N HCl and NaOH. To this solution, HGNR at neutral pH was added and stirred overnight. Purification was performed by ultra-speed centrifugation.

The absorption and emission spectra of the developed nanomaterials were monitored. The characteristic plasmon absorption peaks of GNR broaden and merge to an unresolved single peak on HCl treatment. It may be due to the removal of CTAB from these facets of GNR and probable morphological changes that could have occurred (Fig. 1a).

The formation of specific architectonics by the lateral assembly of individual GNRs is confirmed in the TEM image (Fig. 2a) supporting the observed broadening of the absorption peak. When GQCs at different pH values were treated with neutral HGNR, a drastic change in the surface plasmon absorption peaks (Fig. 1a) was observed. In all the three batches of samples, absorption spectra showed three plasmon peaks with varying intensity (Fig. 1a, inset). When acidic GQC was treated with HGNR, the interaction did not lead to the formation of a hybrid nanomaterial. This is evident from the presence of GQC and GNR separately in the TEM image of AGQC@GNR (Fig. 2b), and confirms its non-assembly at acidic pH. But at the same time, the reaction conditions favoured the breaking of the lateral assembly of HGNR which resulted in the appearance of SPR, characteristic of GNR (Fig. 1a). Moreover, a change in the size of HGNR after the reaction with GQC was also observed (Fig. 2). This change in the size is correlated with the appearance of a doublet peak in the longitudinal SPR region (Fig. 1a, inset). Here, though GQC and GNR are visible separately in the TEM grid, GQC is seen as an entrapped like aggregated material (Fig. 2b, inset), whereas in the case of NGQC@GNR, though the lateral assembly is persistent, it is no longer the same as in the case of HGNR. Distinct separation is maintained between individual gold nanorods while maintaining the lateral assembly as observed in the TEM images (Fig. 2c) than HGNR. Apart from this, the gold clusters were not observed separately in the TEM image. So, the presence of GQC is expected in the close proximity of

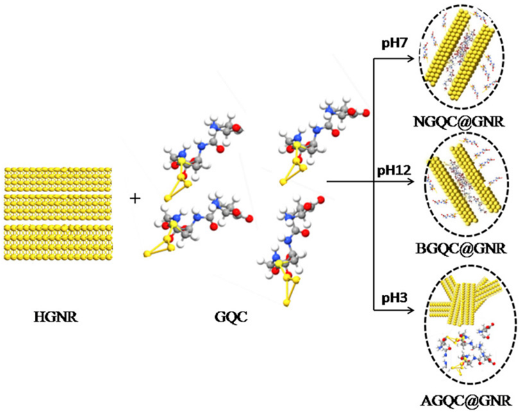

Scheme 1 Synthesis of a hybrid material from GNR and GQC.

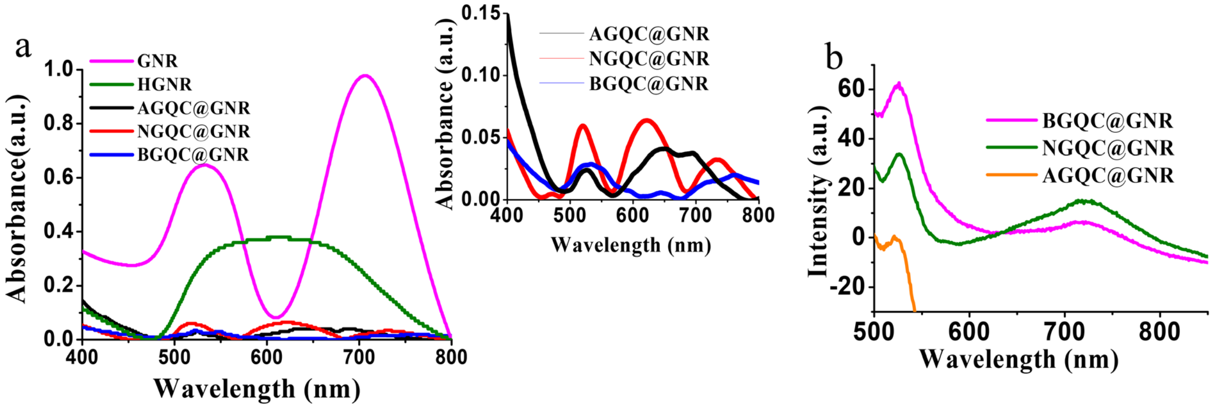

Fig. 1 Absorption (a) and emission spectra (b) of GNR, HGNR, AGQC@GNR NGQC@GNR and BGQC@GNR.

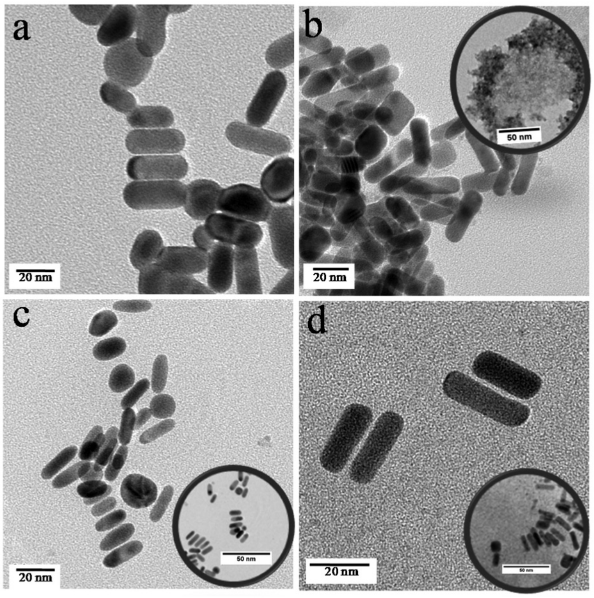

Fig. 2 Transmission electron micrographs of HGNR (a), AGQC@GNR (b) NGQC@GNR (c) and BGQC@GNR (d). The scale bar of all the images is 20 nm and for the inset figures, it is 50 nm.

GNR which resulted in the observed gap between individual GNRs in this case. This observation could be correlated with the observed multiple SPR peaks in the absorption spectra. These multiple absorptions arise from the combined oscillations due to the formation of the unique architectonic of GQC and GNR which behave as a single system in NGQC@GNR (inset of Fig. 2c). Similarly, in the case of BGQC@GNR, GQC can be seen on the surface of GNR and electro statically bound GQCs in the proximity of GNR. In this case, the intra and inter band transitions of gold in GQC and GNR resulted in the observation of shoulder peaks (598 nm and 645 nm) (Fig. 1a, inset) even after breaking the laterally assembled architecture of HGNR by GQC. In both NGQC@GNR and BGQC@GNR, where GQC was added at neutral pH and basic pH, respectively, glutathione has a tendency to exhibit its anionic properties that lead to entrapment of GQC in between HGNRs.[46]

The emission properties of all the three samples were studied and correlated with their architectonics as observed in TEM images which have been reconfirmed with computational analysis. In the case of AGQC@GNR, the observed emission was minimum compared to the other two products (Fig. 1b). Quantum yields of the materials were calculated with respect to a standard dye (Nile Blue). It is also evident from the quantum yield calculation that emission of AGQC@GNR was less compared to the other two products (Fig. S3†). It is due to the zwitterionic nature of glutathione at low pH, which enhances the chance of formation of a hydrogen bond.[46] As a result, it will lead to the formation of an aggregate or clump structure (Fig. 2b). In the case of NGQC@GNR and BGQC@GNR, the fluorescence is high compared with AGQC@GNR but less when compared with GQC. The fluorescence quantum yield also confirms the decrease in the fluorescence compared to GQC. It is due to the direct binding of gold of GQC to GNR; the binding was confirmed using theoretical studies also.

Surface functionalization of GQC on HGNR was confirmed using FT-IR and zeta potential measurements. Peak resemblance of GQC over hybrid systems in the FT-IR spectra (Fig. S4†) indicates the presence of GQC in the material. The broadening of the 3444 cm^{-1} peak indicates intermolecular hydrogen bonding in the case of the hybrid material and it is confirmed by the lower wave number shift of the 1736 cm^{-1} peak which is due to the –C=O peak of the –COOH group which participates in hydrogen bonding. Also, a shift in the 1482 cm^{-1} peak indicates the surface functionalization over HGNR (Fig. S4†). Similarly, the 1649 cm^{-1} peak of GQC shifts to a higher wavenumber region on hybrid formation. The zeta potential of +38 mV of HGNR decreases to +15, 2 and 11 mV for AGQC@GNR, BGQC@GNR and NGQC@GNR, respectively, upon addition of negatively charged GQC (−21 mV) (Fig. S5†). The zeta potential indicates that AGQC@GNR and NGQC@GNR are more stable than BGQC@GNR.

The presence of GNR and GQC is evident in the UV-visible absorption spectroscopy and fluorescence spectroscopy. Still the binding mechanism of GNR and GQC in the hybrid was not clear. In order to elucidate the same, a DFT based computational study was performed, as described in the experimental section. The calculated adsorption energies are −2.67 eV for Conf-1 and −2.44 eV for Conf-2, which indicates significantly strong chemisorption between GQC–GSH and the GNR surface. The optimized geometries and the architectonics of Conf-1 and Conf-2 are shown in Fig. S6.† Both Conf-1 and Conf-2 prefer to bind to the GNR surface through the gold atoms of the cluster. However, there can also be a bonding interaction between the Au atom and the O or N atom in GQC–GSH for Conf-1 and Conf-2, respectively. The Au–O and the Au–N distances are 3.01 Å and 2.56 Å, respectively. Conf-1 being the energetically preferred adsorption configuration between the two, the density of states (DOS) of this configuration was calculated. In Fig. 3, we have compared the DOS of free GQC with that of GQC adsorbed on the GNR surface. The states of GQC in Fig. 3(a) have sharp isolated peaks, indicating the molecular nature of free GQC. We see a broadening and mixing of states close to the Fermi energy of the hybrid material GQC@GNR (in Fig. 3(b)). This clearly demonstrates the effective binding between GQC and GNR in the hybrid system. A net charge transfer of 0.33 e^- from GNR to GQC calculated by Bader's analysis[47,48] is indicative of strong chemisorption. The distance between two GNRs in the TEM of NGQC@GNR is due to the presence of GQC in and around the GNR. From the computational study the possible distance is found to be 0.61 nm.

From the observed gap in TEM and theoretical analyses, it is hypothesized that GQC is attached to the gold atom of GNR in case of NGQC@GNR and BGQC@GNR. From the TEM images in Fig. 2c and d, the distance between rods was calcu-

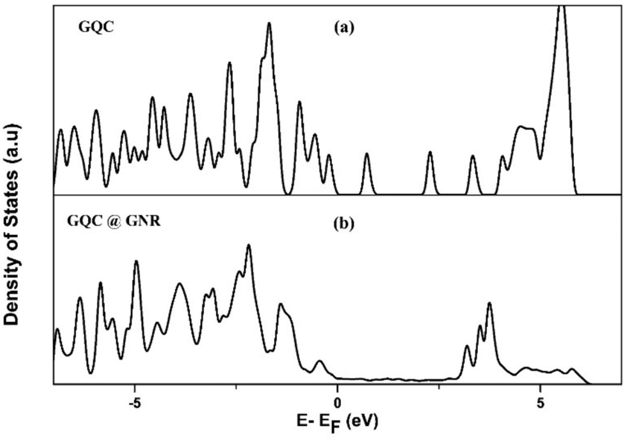

Fig. 3 Density of states (DOS) of free GQC (a) and the GQC@GNR hybrid material (b).

lated and found to be around 0.62 nm with a maximum distance of 1.4 nm agreeing with the theoretical values. The gold–gold interaction as observed by the theoretical studies points to the fact that the distance between the gold cluster and the gold rod is much less. This could be the reason why the cluster is not observed separately in the TEM image in this case. Since both materials of the hybrid system are gold, with equal TEM contrast, to differentiate between them is difficult. However, it is logical to think that the presence of the extended ligands of the cluster pushed the rods apart as compared to HGNR. The presence of GQC over GNR is evident in the high-resolution image, which again clarifies our claim (Fig. S7†). The hydrogen bond formation as observed in the FT-IR analysis of the neighbouring gold cluster plays a vital role in the distance between gold nanorods. Glutathione present in GQC forms an intermolecular hydrogen bond with the neighbouring cluster that leads to a lateral assembly of the hybrid system (Fig. S4†). This hydrogen bond is responsible for the change in the experimental distance as predicted by DFT calculation (0.61 nm).

Looking at the application side of the developed hybrid system, the temperature generation efficacy of the hybrid nanomaterials was evaluated for photothermal therapy application. GQC conjugation resulted in a reduction in the heat generation efficacy of GNR (Fig. S8†). However, there was no significant difference between the temperatures generated by NGQC@GNR and BGQC@GNR. Considering the stability, the fluorescence intensity in the NIR region and the worthy temperature generation efficacy, NGQC@GNR was selected to evaluate its imaging and therapeutic efficacy in cancer cells. To use this hybrid material for the imaging and treatment of cancer, the same material was further conjugated with a cancer targeting molecule, folic acid, to form FA–NGQC@GNR (Scheme S1†). The characteristic absorption peak at 291 nm in the UV-visible absorption spectrum confirms the binding of folic acid. The longitudinal peak of GNR was also present at 707 nm (Fig. S9†), which could be used for plasmonic photothermal therapy. The photothermal efficacy test of FA–NGQC@GNR showed a temperature rise above 40 °C in less than 4 minutes of laser irradiation (Fig. S10†).

The cytotoxicity of folic acid functionalised NGQC@GNR was evaluated both in normal (L929) and cancer (HeLa) cells after 48 h of incubation (Fig. S11†). In the absence of laser irradiation, folate conjugated NGQC@GNR showed high cytocompatibility making it safe to use in biomedical applications (Fig. S11†).

The imaging properties of folate conjugated NGQC@GNR were compared with GNR and GQC in HeLa cells. FA–NGQC@GNR incubated cells in comparison with GNR and control cells (without any material treatment) showed well defined red fluorescence from the cells due to internalisation of FA–NGQC@GNR in HeLa cells (Fig. 4). In the case of GQC, a minimum internalisation occurs due to the passive absorption of small size as well as due to the presence of glutathione in the gold cluster. NGQC@GNR doesn't show much internalization up to 3 h by the cells (Fig. S12†). This could be attributed to the larger size of GQC@GNR than GQC and the lack of target specificity. FA conjugated NGQC@GNR shows more particle uptake within 3 h due to the target specific internalization of the particles by the cells. The absence of fluorescence in the case of non-conjugated material incubated cells is a clear indication of its non-entry into the cells (Fig. S12†). Corresponding nuclear stained images are shown in Fig. S13.† For cellular imaging, green excitation (FITC) and far-red emission (HcRed) filters were used to collect emission in the NIR region using a fluorescence microscope. Interestingly, it is observed that both GQC and FA–NGQ@GNR show fluorescence signals from the nucleus as well. The exact reason is unclear. However, it was reported that materials with molecular weights less than ~40 kDa can passively diffuse into the nucleus.[49]

The therapeutic efficacy of FA–NGQC@GNR, GNR and GQC was evaluated by live/dead assay after incubating the material for 3 h followed by irradiation with an 808 nm laser (Fig. 5). Laser irradiated cells with FA–NGQC@GNR and GNR showed a reduction in cell viability due to the photothermal efficacy of GNR present in both cases. The cell death pattern using these two materials indicates that the hybrid system retains the photothermal properties of GNR in FA–NGQC@GNR. In the case of GQC, there is no effect on laser irradiation and it is similar to that of control cells (Fig. 5).

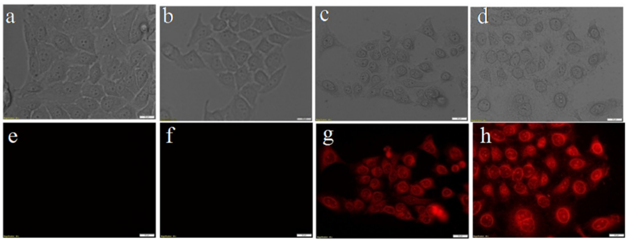

Fig. 4 Cell uptake of FA–NGQC@GNR in HeLa cells. Control cells without any material (a and e), with GNR (b and f), with GQC (c and g) and with FA@GQC–GNR (d and h). Top row images are the bright field images and bottom row images are the fluorescence images.

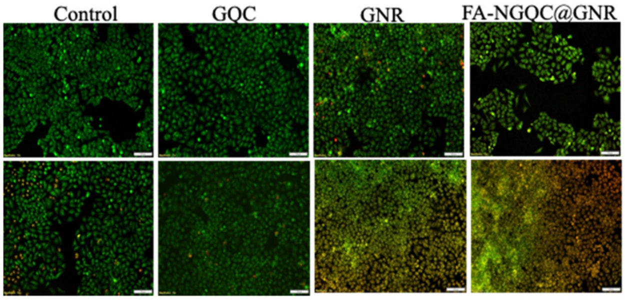

Fig. 5 Live/dead images of HeLa cells incubated with GQC, GNR and FA–NGQC–GNR with (lower panel) and without (upper panel) laser irradiation.

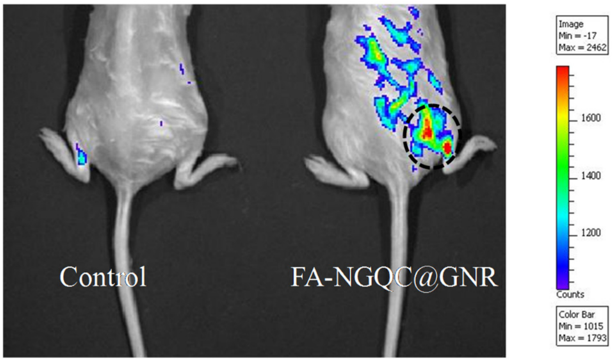

Fig. 7 *In vivo* imaging efficacy of FA–NGQC@GNR.

The photo thermal therapeutic efficacy of FA–NGQC@GNR was quantitatively analysed using MTT assay after incubating for 3 h in HeLa cells. Upon laser irradiation, material incubated cells showed a decrease of cellular viability (Fig. S14†). The PTT mediated cell death was confirmed using Raman spectroscopy.

The Raman bands at ~500 and 663 cm^{-1} (Fig. 6) correspond to disulfide (–S–S–) and carbon–sulfur (–C–S–) vibrations, respectively, of sulfur-containing amino acids in the proteins of live cells. The cells incubated with FA–NGQC@GNR after 808 nm laser exposure show a reduction in the intensity of the –S–S– band, indicating the likely rupture of disulfide bonds due to the PTT effect. The amide III vibrations at 1232 cm^{-1} in the FA–NGQC@GNR treated spectra (without laser) was shifted to 1213 cm^{-1} after laser irradiation due to the conformational changes in the C_6H_5–C stretch of phenylalanine and tyrosine. This shift was accompanied by the enhancement of the in-plane CH bending, ring breathing and in-plane stretching vibrations of the phenylalanine moiety at 1159, 1132, and 1112 cm^{-1}, respectively. The amide I band around 1600 cm^{-1} shifts to a lower region with broadening of the peak due to protein denaturation. The protein and lipid structural vibrations of the untreated cell at 1320 cm^{-1} disappear upon heating, supporting the production of local heat, disrupting the lipid and protein structures leading to cell death.[50–52]

FA–NGQC@GNR was injected intravenously through the tail vein of solid tumor induced mice to evaluate the imaging efficacy of the material *in vivo*. Dalton's lymphoma ascites (DLA) cells were subcutaneously injected to develop tumor in a mouse model.[53] On the 5th day, when the tumor was clearly visible, the hybrid material (FA–NGQC@GNR) was injected through the tail vein. The PBS-injected animals served as controls. All the animals were imaged using an IVIS Spectrum live animal imaging system. The folic acid conjugated hybrid nanomaterial showed greater imaging efficacy in the tumor region due to the targeting towards folate receptor expressed cells and subsequent accumulation of the material in the tumor region (Fig. 7).

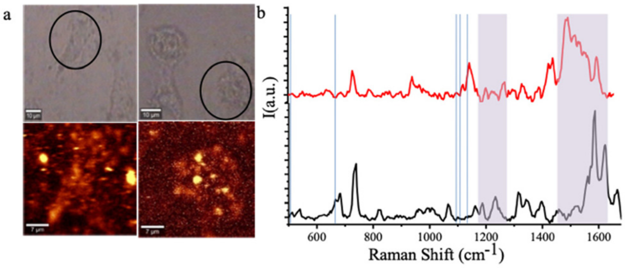

Fig. 6 Raman imaging of HeLa cells treated with FA–NGQC@GNR; with and without laser irradiation (a) and the corresponding Raman spectra of HeLa cells with (red) and without (black) laser irradiation (b).

To confirm the fluorescence signal from the tumor and also to evaluate the biodistribution, animals were sacrificed after 3 h of injection and the organs were imaged with an IVIS Spectrum imaging system (Fig. S15†). It is interesting to see that almost complete targeting of the material in the tumor region is seen, leaving no traces in any other internal organs such as the liver, spleen, heart, lungs, *etc*. High tumor targeting ability and desirable biodistribution endorse this material as a good candidate for *in vitro* cancer imaging and therapy as well as *in vivo* cancer imaging.

Conclusions

In this study, different gold cluster–gold nanorod hybrid systems were developed by adjusting the reaction conditions. Design of metal–metal nanohybrids and their functional properties based on their nanoarchitectonics have been explained experimentally and theoretically. Among them, one of the hybrid materials was selected by considering its fluorescence emission, stability and temperature generation capacity. After folic acid conjugation, the hybrid material showed high therapeutic efficiency *in vitro* due to the target specificity of folate receptors towards cancer cells. The same showed *in vivo* tumor imaging potential as well. In this work, we tried to explore the use of different properties of gold nanomaterials in a single system without compromising the properties of individual nanostructures. We have also shown that the nanoarchitecture of the hybrid significantly influence the optical and thermal properties and hence plays a crucial role in material development for intended applications. Further studies will give new horizons in the field of hybrid nanomaterials and its biomedical applications.

Author contributions

RVN and LVN contributed to idea conception, execution, analysis and manuscript preparation. MFP and RC performed computational analysis. RSJ supervised the overall work and finalized the manuscript.

Conflicts of interest

There are no conflicts to declare.

Acknowledgements

The authors acknowledge the Department of Biotechnology (BT/PR27222/NNT/28/1337/2017) for the financial support. LVN is grateful to DST for the Inspire Faculty Fellowship (IFA18-MS147). RVN is grateful to SERB for NPDF (2020/001274). We thank Dr Sachin J. Shenoy and Mr M. Manoj (SCTIMST) for the help and support provided during the animal experiments. Computational facilities at CCMS, NIT Calicut are gratefully acknowledged.

References

1 K. Ariga, *Nanoscale Horiz.*, 2021, **6**, 364–378.
2 K. Ariga, *Mater. Chem. Front.*, 2017, **1**, 208–211.
3 N. Slepičková Kasálková, P. Slepička and V. Švorčík, *Nanomaterials*, 2021, **11**(9), 2368.
4 D. Maiti, X. Tong, X. Mou and K. Yang, *Front. Pharmacol.*, 2019, **9**, 1–16.
5 C. K. K. Choi, Y. Ting, E. Chiu, X. Zhuo, Y. Liu and C. Y. Pak, *ACS Nano*, 2019, **13**, 5864–5884.
6 C. K. K. Choi, *Nanoscale*, 2017, **9**, 16968–16980.
7 T. Tsukuda, *Bull. Chem. Soc. Jpn.*, 2012, **85**, 151–168.
8 U. Divya Madhuri and T. P. Radhakrishnan, *Dalton Trans.*, 2017, **46**, 16236–16243.
9 N. V. Karimova and C. M. Aikens, *J. Phys. Chem. C*, 2017, **121**, 19478–19489.
10 D. M. Chevrier, *J. Nanophotonics*, 2012, **6**, 064504.
11 H. Qian, M. Zhu, Z. Wu and R. Jin, *Acc. Chem. Res.*, 2012, **45**, 1470–1479.
12 M. Zhou, T. Higaki, Y. Li, C. Zeng, Q. Li, M. Y. Sfeir and R. Jin, *J. Am. Chem. Soc.*, 2019, **141**, 19754–19764.
13 M. A. Abbas, P. V. Kamat and J. H. Bang, *ACS Energy Lett.*, 2018, **3**, 840–854.
14 G. Li and R. Jin, *Acc. Chem. Res.*, 2013, **46**, 1749–1758.
15 K. Ariga and M. Shionoya, *Bull. Chem. Soc. Jpn.*, 2021, **94**, 839–859.
16 A. Gentile, F. Ruffino and M. G. Grimaldi, *Nanomaterials*, 2016, **6**, 1–33.
17 K. L. Kelly, E. Coronado, L. L. Zhao and G. C. Schatz, *J. Phys. Chem. B*, 2003, **107**, 668–677.
18 S. Mej and F. L. Deepak, *J. Nanomater.*, 2012, 1–2.
19 M. A. Raza, Z. Kanwal, A. Rauf, A. N. Sabri and S. Riaz, *Nanomaterials*, 2016, **6**, 1–15.
20 I. Khan, K. Saeed and I. Khan, *Arabian J. Chem.*, 2019, **12**, 908–931.
21 L. Guerrini, R. A. Alvarez-puebla and N. Pazos-perez, *Materials*, 2018, **11**, 1–28.
22 X. Gu, V. Timchenko, G. H. Yeoh, L. Dombrovsky and R. T. Id, *Appl. Sci.*, 2018, **8**, 1–16.
23 V. Nagarajan, T. Chiome and S. Sudan, Springer Cham 2019, pp. 237–244.
24 J. B. Vines, J. Yoon, N. Ryu, D. Lim and H. Park, *Front. Chem.*, 2019, **7**, 1–16.
25 Y. Hong, E. Lee, J. Choi, S. J. Oh, S. Haam, Y. Huh, D. S. Yoon, J. Suh and J. Yang, *J. Nanomater.*, 2012, 1–7.
26 M. A. MacKey, M. R. K. Ali, L. A. Austin, R. D. Near and M. A. El-Sayed, *J. Phys. Chem. B*, 2014, **118**, 1319–1326.
27 Y.-Q. Zhao, Y. Sun, Y. Zhang, X. Ding, N. Zhao, B. Yu, H. Zhao, S. Duan and F.-J. Xu, *ACS Nano*, 2020, **14**, 2265–2275.
28 N. Hlapisi, T. E. Motaung, L. Z. Linganiso, O. S. Oluwafemi and S. P. Songca, *Bioinorg. Chem. Appl.*, 2019, **2019**, 7147128.
29 X. Wang, M. Shao and S. Zhang, *J. Nanopart. Res.*, 2013, **15**, 2–16.
30 F. G. Nanoparticles and T. Biomedical, *Nanomaterials*, 2011, **1**, 31–63.
31 R. V. Nair, H. Santhakumar and R. S. Jayasree, *Faraday Discuss.*, 2018, **207**, 423–435.
32 R. V. Nair, L. V. Nair, D. M. Govindachar, H. Santhakumar, S. S. Nazeer, C. R. Rekha, S. J. Shenoy, G. Periyasamy and R. S. Jayasree, *Chem. – Eur. J.*, 2020, **26**, 2826–2836.
33 B. Hu, L.-P. Zhang, X.-W. Chen and J.-H. Wang, *Nanoscale*, 2013, **5**, 246–252.
34 M. S. Vega, *Nanomaterials*, 2019, **9**, 2–18.
35 A. Gole, J. W. Stone, W. R. Gemmill, H.-C. zur Loye and C. J. Murphy, *Langmuir*, 2008, **24**, 6232–6237.
36 M. Grzelczak, J. Pérez-Juste, F. J. García de Abajo and L. M. Liz-Marzán, *J. Phys. Chem. C*, 2007, **111**, 6183–6188.
37 M. Aioub, S. R. Panikkanvalappil and M. A. El-Sayed, *ACS Nano*, 2017, **11**, 579–586.
38 L. V. Nair, R. V. Nair, S. J. Shenoy, A. Thekkuveettil and R. S. Jayasree, *J. Mater. Chem. B*, 2017, **5**, 8314–8321.
39 L. V. Nair, R. V. Nair and R. S. Jayasree, *Dalton Trans.*, 2016, **45**, 11286–11291.
40 R. A. Vargas-Hernández, *J. Phys. Chem. A*, 2020, **124**, 4053–4061.
41 G. Kresse and J. Hafner, *Phys. Rev. B: Condens. Matter Mater. Phys.*, 1993, **47**, 558–561.
42 J. P. Perdew, K. Burke and M. Ernzerhof, *Phys. Rev. Lett.*, 1996, **77**, 3865–3868.
43 P. Hao, Y. Fang, J. Sun, G. I. Csonka, P. H. T. Philipsen and J. P. Perdew, *Phys. Rev. B: Condens. Matter Mater. Phys.*, 2012, **85**, 1–9.

44 K. Hu, M. Wu, S. Hinokuma, T. Ohto, M. Wakisaka, J. I. Fujita and Y. Ito, *J. Mater. Chem. A*, 2019, **7**, 2156–2164.

45 L. V. Nair, D. S. Philips and R. S. Jayasree, *Small*, 2013, **9**, 2673–2677.

46 E. Moaseri, J. A. Bollinger, B. Changalvaie, L. Johnson, J. Schroer, K. P. Johnston and T. M. Truskett, *Langmuir*, 2017, **33**, 12244–12253.

47 W. Tang, E. Sanville and G. Henkelman, *J. Phys.: Condens. Matter*, 2009, **21**, 21–23.

48 R. F. W. Bader, *Chem. Rev.*, 1991, **91**, 893–928.

49 D. H. Lin and A. Hoelz, *Annu. Rev. Biochem.*, 2019, **88**, 725–783.

50 S. Zong, Z. Wang, J. Yang and Y. Cui, *Anal. Chem.*, 2011, **83**, 4178–4183.

51 I. Notingher, *Sensors*, 2007, **7**, 1343–1358.

52 M. Aioub and M. A. El-Sayed, *J. Am. Chem. Soc.*, 2016, **138**, 1258–1264.

53 K. Jibin, J. S. Prasad, G. Saranya, S. J. Shenoy, K. K. Maiti and R. S. Jayasree, *Biomater. Sci.*, 2020, **8**, 3381–3391.